

THEORETICAL DERIVATION AND ANALYSIS OF THE TRANSFER FUNCTION FOR A HEAT FLUX SENSOR BASED ON ONE-DIMENSIONAL HEAT CONDUCTION

Xuehui Zhang, Deren Kong, Chundong Xu

Nanjing University of Science and Technology, School of Mechanical Engineering, Nanjing, 210094 China (✉ xuehuizhang@njust.edu.cn)

Abstract

The dynamic response characteristics of sensors in heat flux measurement such as rising time and frequency band width, determine the capture ability and measurement error of transient thermal load. In order to quantitatively evaluate the dynamic response characteristics of heat flux sensor, including rise time and frequency band width, based on the differential equation constructed by one-dimensional heat conduction, the analytical expression of the temperature difference between the front and rear surfaces of the sensor sensitive element is derived. Furthermore, the heat flux-temperature transfer function model is established by differential operation and Laplace transform, and the amplitude-frequency response characteristics of the system are analyzed accordingly. The theoretical analysis results are verified by finite element simulation, and the dynamic analysis characteristics of two types of heat flux sensors are analyzed. Finally, the dynamic performance index of the plug calorimeter with adiabatic rear wall is defined. The modeling method and quantitative conclusion put forward in this study provide theoretical basis for the dynamic characteristic optimization and system design of high-precision heat flux sensors.

Keywords: heat flux measurement, dynamic response, frequency band width, one-dimensional heat conduction.

1. Introduction

As an important parameter to characterize the heat transfer per unit area in unit time, the measurement and application of the heat flux have been widely concerned in the research and development of energetic materials and aerospace fields in recent years [1-3].

In these application scenarios, the heat flux changes rapidly, reaching the peak in a few milliseconds, which puts strict demands on the dynamic performance of measurement. In order to improve the dynamic response of heat flux measurement, transient heat flux sensors usually adopt non-water cooling difference layered structure, and measure the temperature gradient of components with known thermal properties (such as thermal conductivity, specific heat capacity, density and geometry) to quantify the heat flux absorbed by the sensitive surface [4-6]. The heat flux sensor based on thin film thermopile and the heat flux sensor based on atomic layer thermopile are representative examples of transient sensors with fast response ability.

Thin-film thermal resistance heat flux sensor is a variant of Schmidt-Bolter heat flux sensor, which calculates the heat flux by the temperature difference between the front and back surfaces of the thermal resistance layer [7-10]. Since the thinner thermal resistance layer corresponds to better dynamic characteristics, the thermal resistance layer with micron thickness is deposited on the millimeter thickness substrate by micromachining process, and the surface temperature difference between the two sides of the thermal resistance layer is measured by thermopile. The thermal resistance layer is usually made of low thermal conductivity materials, such as SiO₂, while the substrate is made of ceramic materials, such as alumina or aluminum nitride. This configuration makes the response time of the sensor in the order of microseconds.

The transient heat flux sensor of atomic layer thermopile also works according to the principle of one-dimensional heat conduction in solid. Specifically, this can be achieved using materials [11–13] whose thermal resistance layer has lateral Seebeck effect, such as YBCO [4, 14] or PbTe. The transverse voltage generated in the thermal resistance layer is perpendicular to the temperature gradient. The atomic layer thermopile film plays a dual role of thermal resistance layer and temperature difference signal output, without additional temperature sensitive elements. Therefore, the thickness of the thermal resistance layer can be kept at sub-micron level (hundreds of nanometers)

The reported research on transient heat flux sensor mostly focuses on structural design and static calibration [15–18]. Basic analysis is usually based on Fourier law of heat conduction, which defines heat flux as the product of temperature gradient and thermal conductivity [19, 20]. But the boundary conditions in the process of heat flux measurement are rarely considered, and there is still a lack of a general theoretical model to quantify the dynamic characteristics. The dynamic response parameters, such as rise time and frequency bandwidth, directly determine the sensor's ability to capture transient thermal load and its measurement accuracy, so they are very important for sensor design and application [21-23]. In this paper, the dynamic response characteristics of heat flux sensor are based on temperature gradient are studied by analyzing one-dimensional heat conduction in solid. By introducing the boundary conditions with heat flux measurement, the differential equation is established and the transfer function of the system is derived. The dynamic behavior in the process of heat flux measurement is further analyzed by finite frequency domain response. The proposed dynamic characteristic modeling framework provides a quantifiable design guide for the structure of high-precision heat flux sensor.

The organization of this paper is as follows: In the second section, the principle and mathematical model of heat flux sensor based on temperature gradient are expounded. In the third section, the temperature distribution of sensitive elements under step heat flux input is solved, and the system transfer function is obtained. In section 4, the dynamic characteristics of two typical heat flux sensor configurations are analyzed.

2. Principle of heat flux measurement based on temperature gradient

The sensitive part of a heat flux sensor typically comprises a thermal resistance layer flanked by thermoelectric conversion elements. The thermal resistance layer transforms the absorbed heat flux into a temperature gradient, that is, the temperature difference between its two sides. The thermoelectric conversion elements are typically implemented using thin-film thermopiles or thin-film thermistors to convert temperature signals into measurable electrical signals. Given that the thermoelectric elements are much thinner than the thermal resistance layer, their thermal influence is negligible. Accordingly, the term "sensitive element" in this paper specifically refers to the thermal resistance layer. Based on the above simplification, the basic structure of the heat flux sensor based on one-dimensional temperature gradient is shown in Fig. 1. The sensitive element is usually made of metal or ceramic materials, the front surface of which is subjected to time-varying thermal load through radiation or convection energy transfer mechanism, and the back side is an adiabatic boundary. By measuring the axial temperature gradient of the sensitive element, the time-varying heat flux $q(t)$ absorbed by the front surface is inferred.

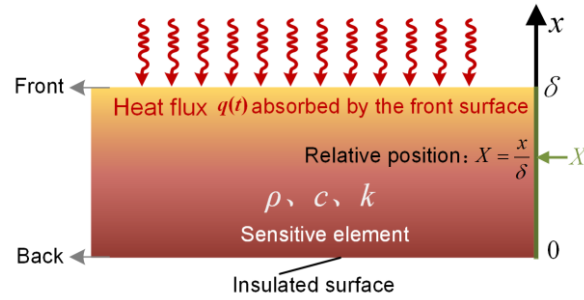


Fig. 1. Schematic diagram of heat flux measurement model based on temperature gradient.

In Fig. 1 where k denotes the thermal conductivity of the sensitive element [$W/(m \cdot K)$]; ρ is the density [kg/m^3]; c denotes the specific heat capacity [$J/(kg \cdot K)$]; α is the thermal diffusivity $\alpha = k/\rho c$ [m^2/s]; δ is the thickness of sensitive element [m]; $q(t)$ represents the heat flux absorbed by the front surface [W/m^2]; X is the is a dimensionless number, which is the ratio of the axial position (x) to the thickness of the sensitive element.

The partial differential equation describing the above heat transfer process is as follows:

$$\frac{\partial T(x,t)}{\partial t} = \alpha \frac{\partial^2 T(x,t)}{\partial x^2}, (0 \leq \delta, 0 \leq t). \quad (1)$$

The boundary condition of the front surface of the sensitive element is modeled as:

$$k \frac{\partial T(x,t)}{\partial x} \Big|_{x=\delta} = q(t). \quad (2)$$

Conversely, the back-surface boundary condition of the sensitive element is modeled as:

$$\frac{\partial T(x,t)}{\partial x} \Big|_{x=0} = 0 \quad (3)$$

The initial conditions of the heat conduction process is:

$$T(x, 0) = T_0. \quad (4)$$

The (1) through (4) jointly satisfies the principles of homogeneity and superposition. Assuming that the thermal properties of the sensitive elements do not change with temperature, this dual satisfaction of linearity and time invariance makes the system a *linear time-invariant* (LTI) system. Therefore, the dynamic characteristics of the system can be fully represented by the transfer function.

3. Transfer function

For the transfer function model of uncooled calorimeters based on temperature gradients, the input is the heat flux absorbed by the front surface of the sensitive element, and the output is the temperature difference between two distinct axial cross-sections. This input-output relationship enables the derivation of the measurement system's transfer function, which quantifies the system's dynamic response to thermal excitation. The transfer function is derived through the following three-step procedure:

- 1) The step response is first obtained by calculating the transient temperature distribution under a step heat flux excitation.
- 2) The impulse response is then derived by differentiating the step response.
- 3) Finally, the transfer function is obtained by applying the Laplace transform to the impulse response.

3.1. Solution of equation under constant heat flux boundary condition

Replace the time-varying heat flux of the front surface with a constant heat flux, that is $q(t) = q_0$, solve the partial differential (1) by separating variables. Define dimensionless quantities: relative temperature θ , relative position X and Fourier number Fo :

$$\theta = \frac{k(T-T_0)}{(q_0\delta)}, X = \frac{x}{\delta}, Fo = \frac{\alpha t}{\delta^2}. \quad (5)$$

Equations (1) to (4) are transformed into (6) to (9), respectively:

$$\frac{\partial \theta(X, Fo)}{\partial Fo} = \frac{\partial^2 \theta(X, Fo)}{\partial X^2}, \quad (6)$$

$$\frac{\partial \theta}{\partial X} \Big|_{X=0} = 0, \quad (7)$$

$$\frac{\partial \theta}{\partial X} \Big|_{X=1} = 1, \quad (8)$$

$$\theta(X, 0) = 0. \quad (9)$$

The solution of (6) that is, (10), establishes an explicit analytical relationship between dimensionless temperature θ and Fourier number Fo .

$$\theta(X, Fo) = \frac{k(T-T_0)}{q\delta} = Fo + \frac{X^2}{2} - \frac{1}{6} + \sum_{n=1}^{\infty} \frac{2}{k_n^2} (-1)^{n+1} \cos(k_n X) e^{-k_n^2 Fo}, \quad (10)$$

where $k_n = n\pi$ ($n = 1, 2, \dots, n$).

The relationship between the dimensionless temperature θ and Fourier number Fo is illustrated in Fig. 2.

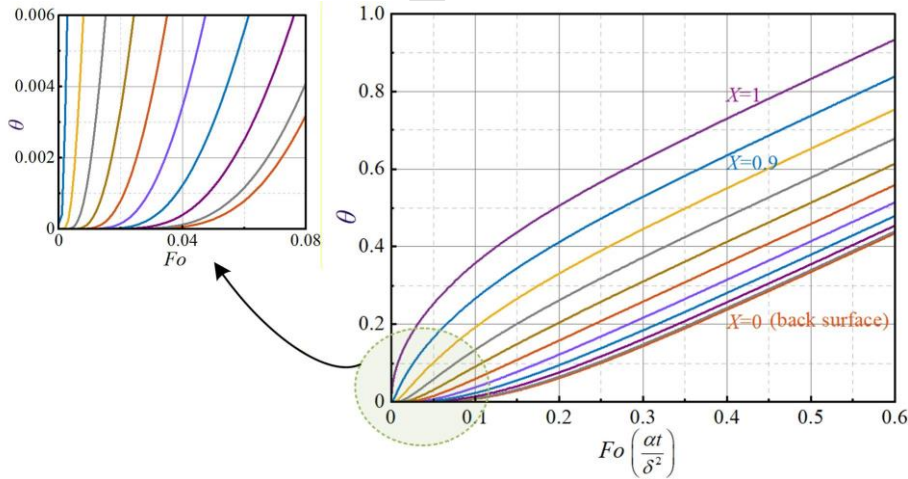


Fig. 2. Relationship between relative temperature and Fourier number.

Furthermore, by substituting the defined dimensionless number (5) into (10), the temperature distribution of the sensitive element is obtained:

$$T(x, t) = T_0 + \frac{q_0\delta}{k} \left[\frac{\alpha t}{\delta^2} + \frac{1}{2} \left(\frac{x}{\delta} \right)^2 - \frac{1}{6} + \frac{2}{\pi^2} \sum_{n=1}^{\infty} \frac{(-1)^{n+1}}{n^2} e^{-(n\pi)^2 \frac{\alpha t}{\delta^2}} \cos \left(n\pi \frac{x}{\delta} \right) \right]. \quad (11)$$

Heat flux at different positions are obtained by differentiating (11) according to the Fourier law of heat conduction:

$$\frac{\partial T}{\partial x} = \frac{q_0}{k} \left[\frac{x}{\delta} - \frac{2}{\pi} \sum_{n=1}^{\infty} \frac{(-1)^{n+1}}{n} e^{-(n\pi)^2 \frac{\alpha t}{\delta^2}} \sin \left(n\pi \frac{x}{\delta} \right) \right] \quad (12)$$

For $Fo < 0.04$, temperature of the back surface of the sensitive element hardly changes ($\theta(0,0.04) \approx 2.9 \times 10^{-5}$), indicating that the front surface heat flux exerts negligible influence on the back surface. When Fo exceeds 0.6, the system achieves a regular regime where both the temperature rise rate and heat flux remain consistent. Fig. 3 illustrates the spatial distributions of temperature and heat flux within the sensitive element under this regular regime.

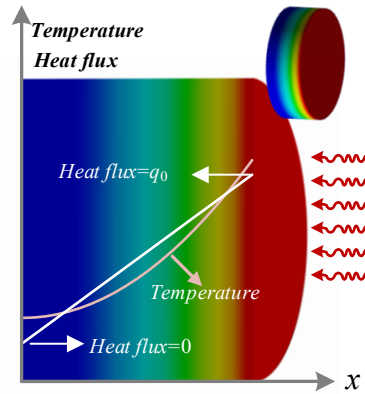


Fig. 3. Distribution of temperature and heat flux after transient heat transfer enters the regular regime.

3.2. Transfer function of the system

By substituting $x = X\delta$ into (11), the temperature distribution at the relative position is derived as follows:

$$T(X, t) = T_0 + \frac{q_0\delta}{k} \left[\frac{\alpha t}{\delta^2} + \frac{1}{2} X^2 - \frac{1}{6} + \frac{2}{\pi^2} \sum_{n=1}^{\infty} \frac{(-1)^{n+1}}{n^2} e^{-(n\pi)^2 \frac{\alpha t}{\delta^2}} \cos(n\pi X) \right]. \quad (13)$$

The temperature difference $\Delta T(X_1, X_2, t)$ between X_1 and X_2 is:

$$\Delta T(X_1, X_2, t) = \frac{q_0\delta}{k} \left[\frac{1}{2} (X_1^2 - X_2^2) + \frac{2}{\pi^2} \sum_{n=1}^{\infty} \frac{(-1)^{n+1}}{n^2} e^{-(n\pi)^2 \frac{\alpha t}{\delta^2}} (\cos(n\pi X_1) - \cos(n\pi X_2)) \right]. \quad (14)$$

Further, the temperature difference of the system under unit heat flux input is as follows:

$$\Delta T_u(X_1, X_2, t) = \frac{\delta}{k} \left[\frac{1}{2} (X_1^2 - X_2^2) + \frac{2}{\pi^2} \sum_{n=1}^{\infty} \frac{(-1)^{n+1}}{n^2} e^{-(n\pi)^2 \frac{\alpha t}{\delta^2}} (\cos(n\pi X_1) - \cos(n\pi X_2)) \right]. \quad (15)$$

In (15), when $t \rightarrow \infty$ or $Fo > 0.6$, the steady-state value is only determined by the non-decaying linear term, and $\Delta T_u(X_1, X_2, \infty)$ represents the steady-state response of the system to the unit heat flux, that is, the sensitivity of the system is shown in (16).

$$\Delta T_u(X_1, X_2, \infty) = \frac{\delta}{2k} (X_1^2 - X_2^2). \quad (16)$$

The unit impulse response of the system is obtained by taking the derivative of (16):

$$\frac{d(\Delta T_u)}{dt} = \frac{2\alpha}{k\delta} \sum_{n=1}^{\infty} (-1)^n e^{-(n\pi)^2 \frac{\alpha t}{\delta^2}} (\cos(n\pi X_1) - \cos(n\pi X_2)). \quad (17)$$

Laplace transformation is performed on (17), and the transfer function of the system is obtained as follows:

$$H(s) = \mathcal{L} \left\{ \frac{d(\Delta T_u)}{dt} \right\} = \frac{2\alpha}{k\delta} \sum_{n=1}^{\infty} \frac{(-1)^n (\cos(n\pi X_1) - \cos(n\pi X_2))}{s + \frac{\alpha(n\pi)^2}{\delta^2}}. \quad (18)$$

Equation (18) shows that the transfer function of the system is a series composed of countless first-order systems. If the first N terms are truncated, the following equation is obtained:

$$H(s) = \frac{2\alpha}{k\delta} \sum_{n=1}^N \frac{(-1)^n (\cos(n\pi X_1) - \cos(n\pi X_2))}{s + \frac{\alpha(n\pi)^2}{\delta^2}}. \quad (19)$$

Essentially, the transfer function can only describe the dynamic behavior of the system strictly when N tends to infinity. But considering the resource consumption in calculation and the allowable error in engineering application, it is very important to understand the approximation ability of the model when N takes finite terms. When N increases, more items are included, and the weight of each item is determined by the numerator and denominator. Although the denominator increases with n^2 , it cannot be simply thought that only the first few terms of the series can describe the low-frequency characteristics of the system more accurately, especially when X_1 and X_2 are close, because the molecules of the subitems may amplify some frequency components when N increases.

Substituting $s = 0$ into the transfer function (19) derives (20), which represents the DC gain of the system. It is equal to (16), represents the static proportional relationship between the input signal and the output signal, which is the sensitivity of the system. When $N \rightarrow \infty$

$$H(0) = \frac{\delta}{2k} (X_1^2 - X_2^2). \quad (20)$$

4. Frequency characteristics of the system

Letting $s = j\omega$ in (19), the frequency response is derived as (21):

$$H(j\omega) = \frac{2\alpha}{k\delta} \sum_{n=1}^N \frac{(-1)^n (\cos(n\pi p_1) - \cos(n\pi p_2))}{j\omega + \frac{\alpha(n\pi)^2}{\delta^2}}. \quad (21)$$

Further, the amplitude-frequency characteristic and phase-frequency characteristic equations of the system are obtained as shown:

$$|H(j\omega)| = \left| \frac{2\alpha}{k\delta} \sum_{n=1}^N \frac{(-1)^n (\cos(n\pi p_1) - \cos(n\pi p_2))}{j\omega + \frac{\alpha(n\pi)^2}{\delta^2}} \right| \quad (22)$$

$$\angle H(j\omega) = \arg \left(\frac{2\alpha}{k\delta} \sum_{n=1}^N \frac{(-1)^n (\cos(n\pi p_1) - \cos(n\pi p_2))}{j\omega + \frac{\alpha(n\pi)^2}{\delta^2}} \right) \quad (23)$$

For any dynamic measurement system, it should be used under the condition of meeting the requirements of undistorted measurement, that is, its amplitude-frequency response should be constant and its phase-frequency response should be linear in a certain frequency band. Generally, the bandwidth of the system is quantized with -3dB bandwidth, which indicates the frequency range when the amplitude of the frequency response drops to $1/\sqrt{2}$ of the maximum.

In the following section, the dynamic responses of two representative heat flux sensor configurations are analyzed. The first configuration ($X_1 = 1$ & $X_2 = 0$) determines the heat flux by measuring the surface temperature gradient across the sensitive element, this is essentially an extension of the slug calorimeter, which the heat flux is inferred from the change rate of the sensitive element's backsurface temperature. The second configuration (X_1 & X_2 is close to 1) represents the thermal gradient quantization in shallow depth (usually < 100 microns), and this is the typical feature of modern thin film heat flux sensor. It should be noted that these two types of heat flux sensors are designed for measuring spatial heat flux, rather than the actual heat transfer rate to the target object which the heat flux sensor thermal resistance should be

close to or (ideally) match the thermal resistance of the material it is mounted on or embedded in.

4.1. Temperature difference between front and back surfaces of the sensitive element.

Closed-loop Nyquist diagram can show the gain and phase information of the system at different frequencies, while Bode diagram shows the amplitude-frequency and phase-frequency characteristics respectively. Combining the two can comprehensively evaluate the system performance. Assuming that the sensitive element material is copper and the material parameters are listed in Table 1.

Table 1. Thermophysical parameters of the copper

k [W/(m · K)]	ρ [kg/m ³]	c [J/(kg · K)]	α [m ² /s]	δ [m]
400	8933	385	1.163×10^{-4}	0.005

The closed-loop Nyquist diagram and Bode diagram of the system are illustrated in Fig. 4 (a) and Fig. 4 (b) respectively when $X_1 = 1$, $X_2 = 0$ and N take different values.

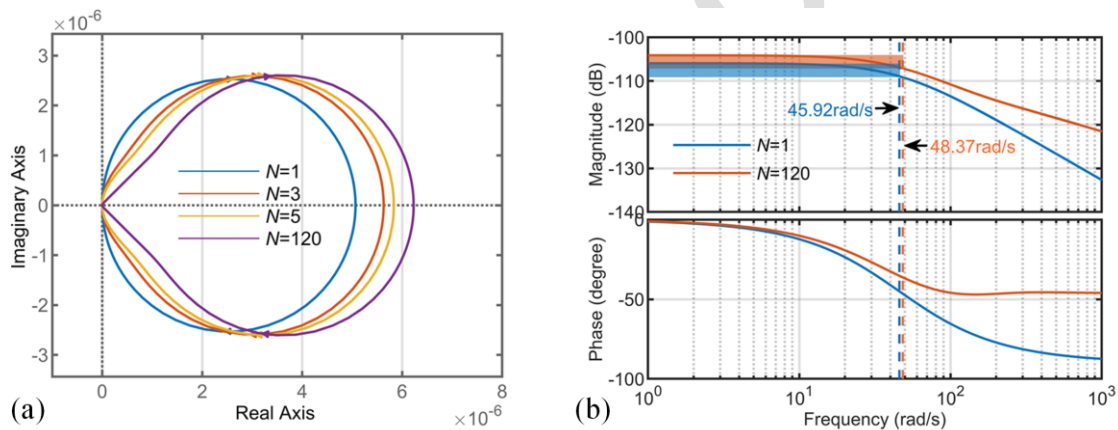


Fig. 4 Frequency characteristics of the system with different values of N : (a) closed-loop Nyquist diagram, (b) bode diagram of the system.

In the Nyquist diagram, when the imaginary axis is 0, the value of the real axis represents the DC gain of the system. Taking the first term of the series $N = 1$, the transfer function is shown in (24):

$$H(s) = \frac{4\delta}{k\pi^2} \frac{1}{1 + \frac{\delta^2}{\alpha\pi^2}s} \quad (24)$$

This system is a typical first-order system, thus its dynamic performance can be characterized by time constant and -3dB bandwidth, the time constant of this system is as follows:

$$\tau = \frac{\delta^2}{\alpha\pi^2} \quad (25)$$

The Fourier number corresponding to the above time constant is:

$$Fo = \frac{1}{\pi^2} = 0.101. \quad (26)$$

The -3dB bandwidth $Bandwidth_{-3dB}$ is:

$$Bandwidth_{-3dB} = \frac{1}{\tau} = \frac{\alpha\pi^2}{\delta^2}. \quad (27)$$

For the material parameters in Table 1, when N is 1, the time constants of the system are as follows:

$$\tau = 128.97ms, \quad (28)$$

$$Bandwidth_{-3dB} = 45.92rad/s. \quad (29)$$

4.1.1. Time domain response of the system under step signal input

The zero-state response of the system can be obtained by (14), which needs to be approximated by infinite series. In order to evaluate the response of the system under step heat flux comprehensively, Ansys Workbench Transient Thermal Analysis module (Release 2020 R2) is used for simulation. The sensitive element is defined as a three-dimensional plate, 15 [mm] in diameter and 5 [mm] in thickness, and is composed of copper; its thermophysical parameters are listed in Table 1. A hex-dominant meshing scheme is adopted, with local refinement applied to the front surface where the heat flux is loaded, in order to accurately resolve the thermal gradient. The mesh layout and the simulated temperature distribution are presented in Fig. 5. The global element size is controlled by the solver with adaptive sizing enabled. The resulting mesh consists of 46355 nodes and 6807 cells. A step heat flux of $q = 1$ [MW/m²] is applied on the front surface, while all other surfaces are treated as adiabatic. The simulation solves the three-dimensional, unsteady Fourier heat conduction equation using the direct time-integration method available in the transient thermal analysis module.

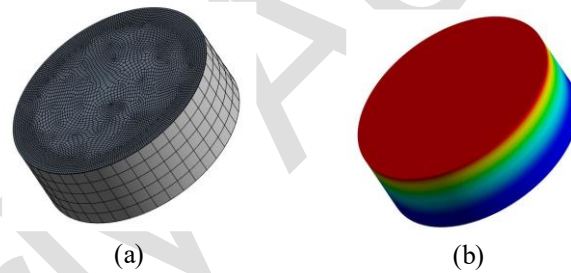


Fig. 5. Grid layout and temperature distribution of simulation model; (a) grid layout of the sensitive element, (b) temperature distribution in sensitive element.

The temperature distribution in the sensitive element is shown in Fig. 6.

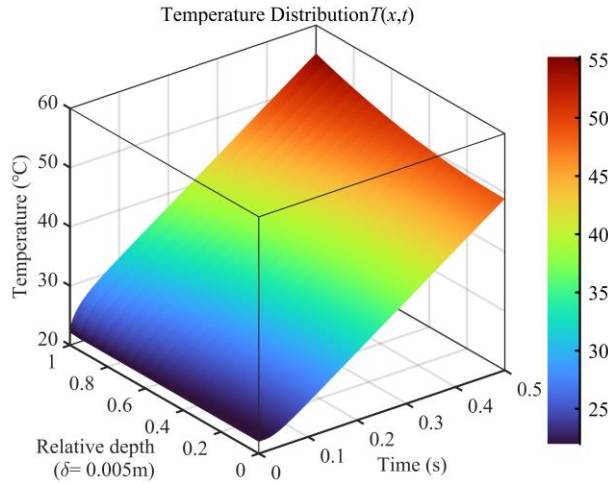


Fig. 6. Temperature distribution under step heat flux input.

When $T_f = T(\delta, t)$, $T_b = T(0, t)$, the simulation results of temperature difference between the front and back surface is shown in Fig. 7.

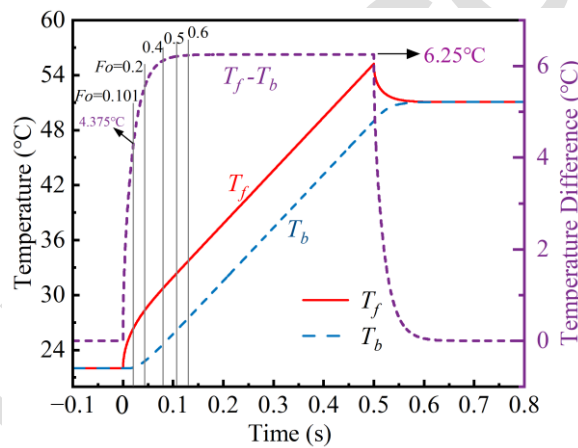


Fig. 7. Simulation results of temperature difference between front and back surfaces.

As illustrated in Fig. 7, with time increasing, the temperature distribution in the sensitive element gradually stabilizes into a regular regime state. When the Fourier number exceeds 0.6, the temperature difference between the front and back surface remains constant, with a measured value of 6.25 [°C]:

$$\Delta T(X_1, X_2, \infty) = \frac{q_0 \delta}{2k} = 6.25^\circ\text{C} \quad (30)$$

For the standard first-order system, the step response of the system at the time constant is 0.707 of the steady-state value, while according to the simulation results, the step response of the system at the time constant is 0.7, which reflects the slight error caused by the truncation of the transfer function.

4.1.2. Response of the system under periodic signal input

When sinusoidal heat flux excitation as shown in (31) is applied to the front surface of the sensitive element:

$$q_{sin}(t) = q_0 \sin[(\omega_{-3dB})t] \tag{31}$$

Let $\omega_{-3dB} = 45.92$ [rad/s], which is the calculation result of (29). Temperature and temperature difference between the front and rear surfaces of the system, and curves between temperature difference and input heat flux are shown in Fig. 7a and Fig. 7b respectively.

As illustrated in Fig. 8b, at the steady-state stage, the expression of temperature difference between the front and rear surfaces is as follows:

$$T_f - T_b = 4.5 \times \sin[45.92(t - 0.0134)] \tag{32}$$

Based on the analysis of the derived model, the output of the system shows 0.0134 [s] output delay and 0.614 [rad] phase shift (equivalent to 35°) relative to the input heat flux. The phase obviously deviates from the value of the first-order system 45° , indicating that the phase distortion caused by the system approximation exceeds the amplitude distortion.

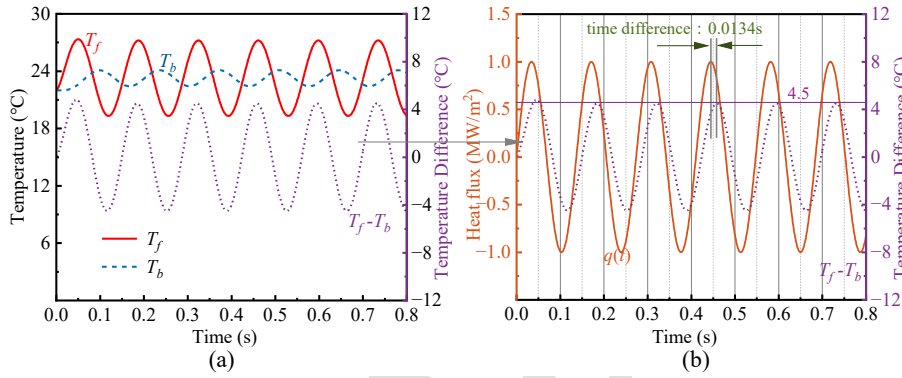


Fig. 8. Temperature difference of the system when the front surface is dynamic heat flux; (a) temperature and temperature difference between the front and back surfaces, (b) phase correlation between the heat flux of the front surface and the temperature difference between the front and back surfaces.

The frequency characteristics of the system under varying parameter N at $\omega = 45.92$ [rad/s] are quantitatively summarized in Table 2.

Table 2. Amplitude and phase of the system with different values of n when the angular frequency is 45.92 rad/s.

Truncation number	Frequency [rad/s]	Magnitude $\times 10^{-6}$	Phase [degree]
$N=1$	45.92	3.58	-45
$N=120$	45.92	4.52	-35.25
Ansys simulation	45.92	4.5	-35.15

The analytical findings demonstrate that with the increase of N , the -3dB bandwidth of the system gradually widens, the DC gain gradually increases, and the phase corresponding to the -3dB bandwidth gradually decreases. Numerical simulation shows that the fidelity of numerical calculation data is higher than that of first-order model approximation. Nevertheless, when the first-order modal approximation is applied to the transfer function, the system bandwidth becomes narrower than the actual -3dB bandwidth. This indicates that the approximated system demonstrates superior amplitude-frequency characteristics compared to the physical system. Therefore, -3dB bandwidth derived from the first-order modal approximation can effectively characterize the system's dynamic performance.

4.2. Shallow resistance heat flux sensor

In this case, a thermal resistance layer with low thermal conductivity is usually deposited on a high thermal conductivity substrate, as shown in Fig. 9. In order to simplify the analysis of the dynamic response of the system, it is assumed that the thermal resistance layer and the substrate have the same material characteristics.

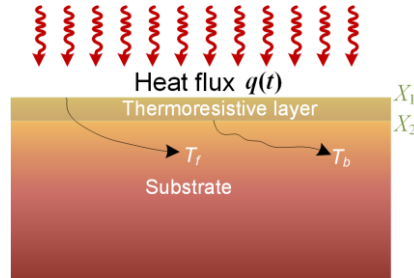


Fig. 9. Schematic diagram of sensor with substrate.

For this kind of structure, $X_1 = 1$, and X_2 is a value close to 1, since the thermal resistance layer is generally thin. When $X_2 = 0.99$, the step response is shown in Fig. 10. Frequency response characteristics of different values of N are shown in the Fig. 11.

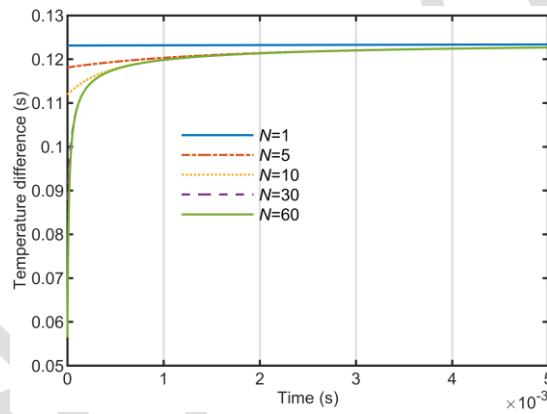


Fig. 10. Step response with different values of N .

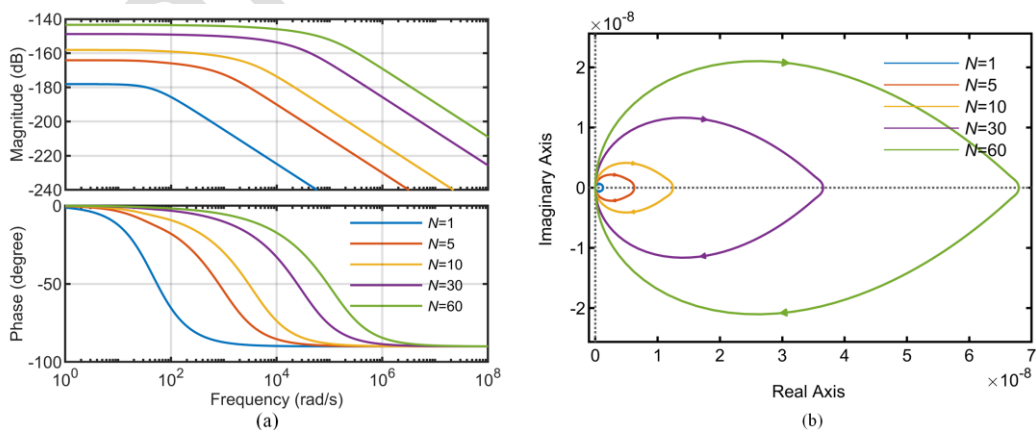


Fig. 11. Frequency domain response of the system when using different N to approximate the model; (a) bode diagram, (b) closed-loop Nyquist diagram.

Analysis results demonstrate that as the number of participating modes increases, the system's -3dB bandwidth exhibits significant enhancement, at the same time, the DC gain is monotonically increased until reaching the system's theoretical limit:

$$\Delta T(X_1, X_2, \infty) = \frac{q\delta}{2k} (X_1^2 - X_2^2) = 1.24 \times 10^{-7} = -138\text{dB} \quad (33)$$

For $N = 120$, the transient term becomes so small that it underflows the effective range of floating-point numbers, introducing numerical errors, therefore use $N = 60$ to ensure computational stability. Under $N = 60$, the frequency response of the system at different X_2 is shown in Fig. 12. As the thickness of the thermal resistance layer decreases, the system bandwidth gradually increases while the sensitivity continuously diminishes, which means that the temperature difference becomes smaller. To compensate for the diminished signal, multiple thermopiles may be arranged on both sides of the thermal resistance layer. However, this enhancement strategy necessitates balancing improvements in sensitivity with potential increases in response time.

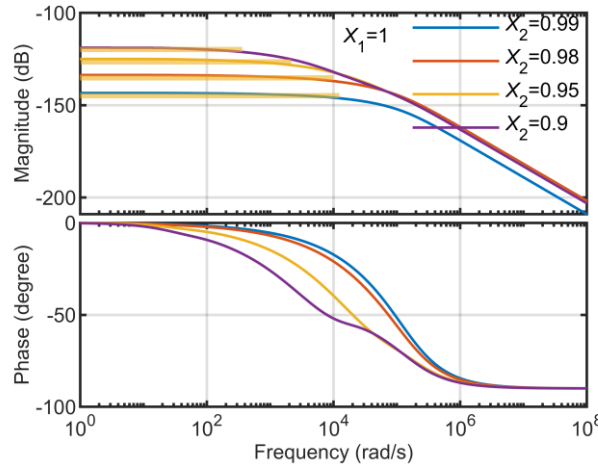


Fig. 2. Bode diagram of thermal resistance layer system with different thickness.

Using the material parameters specified in Table 1 with $N = 60$, Table 3 presents the system bandwidth values corresponding to varying thicknesses of the thermal resistance layer.

Table 3. Bandwidth with different thickness of thermal resistance layer.

X_2	Sensitivity $\times 10^{-7}$ [K/(W/m ²)]	-3dB bandwidth [rad/s]	Phase [degree]
0.99	1.24	13759.46	-20.25
0.98	2.48	8395.36	-19.33
0.95	6.09	1798.84	-19.42
0.9	11.88	553.44	-20.23

The finite-term approximation methodology imposes inherent constraints on transfer function-based bandwidth estimation. Specifically, the actual system bandwidth invariably exceeds the calculated value derived from this truncated model. Nevertheless, sensors employing this structural configuration represent a viable strategy for enhancing dynamic performance.

5. Conclusion

In this study, the dynamic response characteristics of non-cooling heat flux sensor based on one-dimensional temperature gradient are quantified, and the following conclusions are drawn by constructing heat transfer model and system transfer function:

1) The sensitivity of the system can be accurately quantified by solving the DC gain of the transfer function, and the effective working frequency band of the system can be clearly defined by combining the modal decomposition theory to approximate the frequency response, which establishes a mathematical criterion for the design of the frequency response characteristics of the sensor.

2) In the temperature difference measurement mode between absorption surface and insulation surface, the dynamic characteristics of the system can be equivalent to the first-order inertia link, and the distortion of the phase-frequency characteristics of the system is greater than that of the amplitude-frequency characteristics. This simplified model provides a theoretically solvable engineering realization path for transient heat flux measurement.

3) For the heat flux sensor with surface-deep gradient temperature measurement configuration, its high-order modal components have a significant impact on the dynamic response of the system, so the multi-order modal superposition method must be adopted to accurately characterize the essential characteristics of the system. Theoretical analysis shows that this type of structure can increase the bandwidth of the sensor by 1-2 orders of magnitude, which is an effective means to improve the measurement of transient heat flux.

4) Under some complex shapes and boundary conditions, it is difficult to establish and solve the mathematical model of the system, that is, partial differential equations. At this time, finite element simulation tools can be used for auxiliary analysis. Nevertheless, the design methodology of heat flux measurement system presented in this paper emphasizes the matching relationship among material parameters, boundary conditions and spectral characteristics of measured heat flux in many aspects, which is still of reference significance for the design and simulation of this kind of heat flux measurement system.

References

- [1] Murphy, P., Persoons, T., & O'Shaughnessy, S. (2022b). The use of hot film sensors for the heat flux measurement of impinging jet flows: A comparison of postprocessing methods. *Heat and Mass Transfer*, 60(12), 2025–2035. <https://doi.org/10.1007/s00231-022-03297-w>
- [2] Kong, X., Xu, C., Zhang, X., & Li, B. (2022). Testing and evaluation of the thermal damage caused by an explosion of energetic materials. *International Journal of Thermal Sciences*, 186, 108121. <https://doi.org/10.1016/j.ijthermalsci.2022.108121>
- [3] Huang, W., Gong, C., Li, C., & Gou, J. (2023). Real-Time Data-Driven inverse heat conduction method for a reentry flight vehicle based on the Random Forest algorithm. *Journal of Aerospace Engineering*, 37(1). <https://doi.org/10.1061/jaeeez.aseng-5205>
- [4] Huber, K., Rödiger, T., Bhatnagar, L., & Paniagua, G. (2022). Atomic Layer Thermopiles: Comprehensive static calibration, comparison and application in subsonic and supersonic flows. *International Journal of Thermal Sciences*, 183, 107881. <https://doi.org/10.1016/j.ijthermalsci.2022.107881>
- [5] Zribi, A., Barthès, M., Bégot, S., Lanzetta, F., Rauch, J. Y., & Moutarlier, V. (2016). Design, fabrication and characterization of thin film resistances for heat flux sensing application. *Sensors and Actuators a Physical*, 245, 26–39. <https://doi.org/10.1016/j.sna.2016.04.040>
- [6] Miller, R. A., & Alpert, H. S. (2023). Temperature dependent performance of Schmidt–Boelter heat flux sensors. *Review of Scientific Instruments*, 94(2), 025002. <https://doi.org/10.1063/5.0129703>
- [7] Zhang, T., Tan, Q., Lyu, W., Lu, X., & Xiong, J. (2019). Design and fabrication of a thick film heat flux Sensor for Ultra-High Temperature Environment. *IEEE Access*, 7, 180771–180778. <https://doi.org/10.1109/access.2019.2958853>

- [8] Xie, H., Zhang, L., Li, X., Li, S., Hao, Z., Wang, H., Xiong, J., & Tan, Q. (2023). Design, preparation, and performance study of a miniaturized High-Temperature Thick-Film Heat Flux Sensor. *IEEE Sensors Journal*, 23(11), 11420–11427. <https://doi.org/10.1109/jsen.2023.3255919>
- [9] Fu, X., Lin, Q., Peng, Y., Liu, J., Yang, X., Zhu, B., Ouyang, J., Zhang, Y., Xu, L., & Chen, S. (2020). High-Temperature Heat Flux Sensor based on Tungsten–Rhenium Thin-Film Thermocouple. *IEEE Sensors Journal*, 20(18), 10444–10452. <https://doi.org/10.1109/jsen.2020.2993592>
- [10] Doronin, D. O. (2018). Sensors for Metering Heat Flux Area Density and Metrological Equipment for The Heat Flux Density Measurement. *Journal of Physics Conference Series*, 998, 012008. <https://doi.org/10.1088/1742-6596/998/1/012008>
- [11] Liu, S., Zhao, J., & Liu, Z. (2023). A transient heat flux sensor for PbTe thin films based on transverse Seebeck effect. *Measurement Science and Technology*, 34(12), 125122. <https://doi.org/10.1088/1361-6501/acflbe>
- [12] Chen, X., Tao, B., Zhao, R., Yang, K., Li, Z., Xie, T., & Xia, Y. (2024). Fast-Response Thin Film Heat flux sensors for harsh environments. *IEEE Sensors Journal*, 24(12), 18844–18850. <https://doi.org/10.1109/jsen.2024.3393775>
- [13] Liu, Z., Liu, S., Zhao, J., Yue, Y., Xu, Q., & Yang, F. (2022). A transient heat flux sensor based on the transverse Seebeck effect of single crystal Bi₂Te₃. *Measurement*, 198, 111419. <https://doi.org/10.1016/j.measurement.2022.111419>
- [14] Chen, X., Tao, B., Zhao, R., Yang, K., Xia, Y., Wang, Q., Li, Z., & Xie, T. (2023). Angle- and Thickness-Dependent response characteristics of YBA₂CU₃O₇- Δ -Based Atomic-Layer Thermopile heat Flux sensors. *IEEE Sensors Journal*, 23(22), 27053–27058. <https://doi.org/10.1109/jsen.2023.3319391>
- [15] Xu, G., Huang, Y., Dong, B., Quan, Y., Yin, Q., & Chai, J. (2023). Design and performance evaluation of a novel thin-film heat flux sensor. *Case Studies in Thermal Engineering*, 47, 103121. <https://doi.org/10.1016/j.csite.2023.103121>
- [16] Gifford, A., HOFFIE, A., DILLER, T., & HUXTABLE, S. (2009). Convection calibration of Schmidt–Boelter heat flux gauges in stagnation and shear air flow. *Journal of Heat Transfer*, 132(3). <https://doi.org/10.1115/1.3211866>
- [17] Siroka, S., Foley, B. M., Berdanier, R. A., & Thole, K. A. (2021). Application of 3-omega method for thin-film heat flux gauge calibration. *Measurement Science and Technology*, 32(11), 114001. <https://doi.org/10.1088/1361-6501/ac0f23>
- [18] Li, Z., Yin, J., Wang, G., Liang, H., Zhang, C., Huang, M., Liu, Y., & Zhang, J. (2022). Dynamic calibration of a Thin-Film Heat-Flux sensor in time and frequency domains. *Sensors*, 22(14), 5294. <https://doi.org/10.3390/s22145294>
- [19] Freed, M., Kruger, M., Poolla, K., & Spanos, C. (2005). Wafer-Grown Heat flux sensor arrays for plasma Etch processes. *IEEE Transactions on Semiconductor Manufacturing*, 18(1), 148–162. <https://doi.org/10.1109/tsm.2004.840526>
- [20] Xie, S., Zhu, J., Jiang, H., Zhao, X., Liu, B., & Jia, Z. (2024). Preparation and properties of High-Temperature Transient Thin-Film Thermopile Heat Flux Sensor. *Journal of Electronic Materials*, 54(1), 361–369. <https://doi.org/10.1007/s11664-024-11476-0>
- [21] Siroka, S., Berdanier, R. A., & Thole, K. A. (2022). Development of coated heat flux gauges for fast responding measurements. *Measurement Science and Technology*, 33(4), 045104. <https://doi.org/10.1088/1361-6501/ac4638>
- [22] Naveros, I., Ghiaus, C., & Ruíz, D. (2016). Frequency response limitation of heat flux meters. *Building and Environment*, 114, 233–245. <https://doi.org/10.1016/j.buildenv.2016.12.025>
- [23] Woodbury, K. A., & Beck, J. V. (2013). Heat conduction in a planar slab with power-law and polynomial heat flux input. *International Journal of Thermal Sciences*, 71, 237–248. <https://doi.org/10.1016/j.ijthermalsci.2013.04.009>



Xuehui Zhang was born in Binzhou, Shandong, China, in 1995. He received the B.S. degree in measurement and control technology and instrument from Qingdao University of Technology, Qingdao, China, in 2017. He is currently pursuing the Ph.D. degree at Nanjing University of Science and Technology. His main research interests include Transient thermal parameter measurement, Explosion damage test

and Optical radiation measurement.



Chundong Xu received the Ph.D. degree in mechanical manufacture and automation from the Southeast University, Nanjing, China, in 2016. He is currently an Associate Professor with the School of Mechanical Engineering, Nanjing University of Science and Technology, Nanjing. His research interests include static calibration of dynamic pressure measurement systems and motion

parameter tests.



Deren Kong was born in Taizhou, Jiangsu, China, in 1964. He received the B.S., M.S., Ph.D. degree all in mechanical engineering from Nanjing University of Science and Technology, Nanjing, China, in 1990, 1998 and 2003. He is currently a professor with Nanjing University of Science and Technology. His main research interests include the test technology of dynamic parameters of weapons.

Early Access